Mesoscale Eddy–Internal Wave Coupling. Part I: Symmetry, Wave Capture, and Results from the Mid-Ocean Dynamics Experiment

KURT L. POLZIN

Woods Hole Oceanographic Institution, Woods Hole, Massachusetts

(Manuscript received 18 July 2006, in final form 6 December 2007)

ABSTRACT

Vertical profiles of horizontal velocity obtained during the Mid-Ocean Dynamics Experiment (MODE) provided the first published estimates of the high vertical wavenumber structure of horizontal velocity. The data were interpreted as being representative of the background internal wave field, and thus, despite some evidence of excess downward energy propagation associated with coherent near-inertial features that was interpreted in terms of atmospheric generation, these data provided the basis for a revision to the Garrett and Munk spectral model.

These data are reinterpreted through the lens of 30 years of research. Rather than representing the background wave field, atmospheric generation, or even near-inertial wave trapping, the coherent high wavenumber features are characteristic of internal wave capture in a mesoscale strain field. Wave capture represents a generalization of critical layer events for flows lacking the spatial symmetry inherent in a parallel shear flow or isolated vortex.

1. Introduction

Conducted during March–July of 1973, the Mid-Ocean Dynamics Experiment (MODE) was one of the first concentrated studies of mesoscale ocean variability. The experiment featured arrays of moored current meters, neutrally buoyant floats, standard hydrographic station techniques, and the use of novel vertically profiling instrumentation.

Vertical profiles of horizontal velocity obtained with a free-falling instrument using an electric field-sensing technique (Sanford 1975) provided the first published estimates of the high vertical wavenumber structure of horizontal velocity. The data were assumed to be representative of the background internal wave field and thus, despite some evidence of excess downward energy propagation (Leaman and Sanford 1975) that was interpreted in terms of atmospheric generation (Leaman 1976), the data provided the basis for a revision to the isotropic Garrett and Munk (1975) spectral model. These data and their analysis are seminal in their influence of how we think about the oceanic internal wave field.

The point of this paper is to suggest an alternate interpretation of those data—that the high wavenumber contributions are dominated by coherent features characteristic of a "shrinking catastrophe" (Jones 1969) or "wave capture" (Bühler and McIntyre 2005) scenario of internal wave–mesoscale eddy interaction. Wave capture is phenomenologically distinct from a parallel shear flow critical layer (e.g., Jones 1967) or near-inertial internal wave trapping (Kunze 1985).

This interpretation is motivated by recent developments featuring the following results:

- a regional characterization of the background internal wave field rather than the previous universal model (K. Polzin and Y. Lvov 2008, unpublished manuscript);
- revised estimates of net energy transfers between the internal wave field and the mesoscale eddy field that indicate wave–eddy coupling is a significant, if not *the* primary regional source of internal wave energy (Polzin 2008a, manuscript submitted to *J. Phys. Oceanogr.*, hereafter P0a); and
- the development of a heuristic local characterization of internal wave–wave interactions (Polzin 2004) and use of that characterization in a radiation balance scheme (Müller 1976) to quantify the magnitude of the wave–eddy coupling process (Polzin 2008, manu-

Corresponding author address: Kurt L. Polzin, WHOI, MS#21, Woods Hole, MA 02543.
E-mail: kpolzin@whoi.edu

DOI: 10.1175/2008JPO3666.1

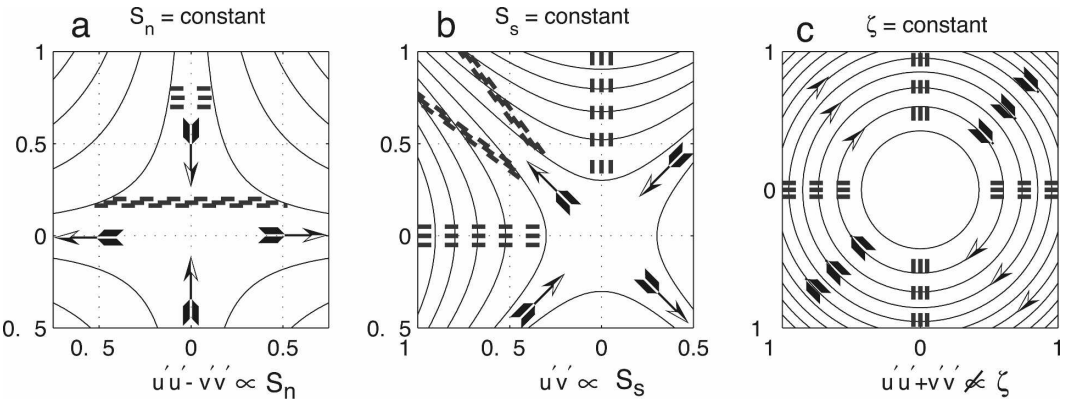

FIG. 1. Phase lines (dashed) of waves being passively advected by three realizations of a steady mean flow having streamlines denoted by the solid contours: (a) a spatially constant deformation strain, (b) a spatially constant shear strain, (c) a spatially constant relative vorticity. Strain results in the filamentation of wave phase. Relative vorticity simply results in a rotation of the wavevector.

script submitted to *J. Phys. Oceanogr.*, hereafter P0b), with the further suggestion that wave–eddy coupling might explain some of the regional variability alluded to above (K. Polzin and Y. Lvov 2008, unpublished manuscript).

The MODE velocity profile data do not fit easily into the regional characterization promoted by K. Polzin and Y. Lvov 2008, unpublished manuscript. In that study, Eulerian frequency (σ) spectra that are whiter (less steep) than σ^{-2} typically accompany vertical wavenumber (m) spectra that are redder (steeper) than m^{-2}. Rather than exhibiting a power law fit, the MODE gradient spectra are peaked at vertical wavelengths smaller than 100 m. This oddball warranted further investigation.

The interpretive context here is that of the Wentzel–Kramers–Brillouin (WKB) approximation and ray tracing within a 3D quasigeostrophic flow field (Bretherton (1966); Jones (1969)). Pertinent results are summarized in the appendix. Internal waves are assumed to be of small amplitude and have small spatial scales relative to a geostrophically balanced background $\overline{\mathbf{u}}(x, y, z)$ that evolves over a much longer time scale. Spatial gradients in the background are assumed to be sufficiently small, such that wave–mean interactions affect wave propagation only through an advective Doppler shift, $\mathbf{k} \cdot \overline{\mathbf{u}}$. Ray tracing features an action ($\mathcal{A} = E/\omega$) conservation statement with variations in intrinsic frequency $\omega = \sigma - \mathbf{k} \cdot \overline{\mathbf{u}}$ being offset by variations in energy (E) following ray paths. It is crucial that the reader be cognizant that wave–mean interactions can be qualitatively different for two- and three-dimensional background flows.

Despite the complexity of a three-dimensional background state, a simple characterization of the interaction is possible. Bühler and McIntyre (2005) point to an analogy between internal wave propagation and the problem of particle pair separation in incompressible 2D turbulence. In this relative dispersion problem, particle pairs undergo exponential separation when the rate of strain exceeds relative vorticity:

$$S_s^2 + S_n^2 > \zeta^2, \tag{1}$$

where $S_s \equiv \overline{v}_x + \overline{u}_y$ is the shear component of strain, $S_n \equiv \overline{u}_x - \overline{v}_y$ is the normal component, and $\zeta \equiv \overline{v}_x - \overline{u}_y$ is relative vorticity. Equation (1) is simply the Okubo–Weiss criterion (e.g., Provenzale 1999). Bühler and McIntyre argue that the problem of small-amplitude waves in a larger-scale flow field is kinematically similar to particle pair separation. If strain dominates vorticity, the ray equations lead to an exponential increase/decrease in the density of phase lines, that is, an exponential increase/decrease in horizontal *wavenumber*, $k_h = (k^2 + l^2)^{1/2}$ (Fig. 1). Vorticity simply tends to rotate the horizontal *wavevector* in physical space. The collapsing of phase lines in an eddy strain field associated with exponential growth provides a simple picture of how an internal wave packet interacts with an eddy strain field.

Jones (1969) and Bühler and McIntyre (2005) further argue for a shrinking catastrophe or wave capture scenario. Simply put, the vertical wavenumber is slaved to the horizontal, so that exponential growth of the horizontal wavenumber implies either exponential growth or decay of the vertical wavenumber in the presence of thermal wind shear. Whether the vertical wavenumber grows or decays depends on the sign of the horizontal wavenumber relative to the thermal wind shear. Those waves with growing horizontal and vertical wavenumber magnitude will tend to be captured within the extensive regions of the eddy strain field and eventually

dissipate: strain acts as a funnel to collect high wavenumber, low intrinsic frequency waves. Asymptotically, a captured wave will tend to

$$\frac{dm}{dt} = \mathbf{k} \cdot \bar{\mathbf{u}}_z \rightarrow m\sqrt{D}, \tag{2}$$

with a corresponding wave aspect ratio

$$\frac{m}{k_h} = \frac{\mathbf{k} \cdot \bar{\mathbf{u}}_z}{k_h\sqrt{D}} \leq \frac{|\bar{u}_z|}{\sqrt{D}}, \tag{3}$$

where $D \equiv (S_n^2 + S_s^2 - \zeta^2)/4$ and the vertical wavenumber is m. This finite aspect ratio implies the captured wave tends to an intrinsic frequency ω *larger* than the Coriolis frequency f. Bühler and McIntyre (2005) refer to wave capture as a nontrivial variant of a critical layer in a two-dimensional flow, which in turn is characterized by linear growth of the cross-stream and vertical wavenumbers. The intrinsic frequency consequently tends to f in the 2D problem. (See the appendix for details.)

The situation envisioned by Jones (1969) and Bühler and McIntyre (2005) is an idealized representation of the oceanic mesoscale for several reasons. First, although there is arguably a scale separation between internal waves and mesoscale eddies, it is not obvious that this scale separation is sufficient for the asymptotic results quoted above to be applicable: wave propagation may result in the termination of a capture event. A second complication is one of time dependence in the slowly evolving mesoscale field. Müller (1976) points out that a resonance condition is possible if the progression of the ray trajectory matches the phase velocity of the mesoscale. Within the thermocline, mesoscale features are observed to migrate westward at a speed of approximately 2 km day^{-1}, or about 2 cm s^{-1}, and somewhat faster (5 cm s^{-1}) at depth (Freeland and Gould 1976). These westward drifts are also typical group velocities for high vertical wavenumber, near-inertial internal waves. Finally, waves with increasing horizontal wavenumber magnitude and decreasing vertical wavenumber magnitude are undergoing transport to higher intrinsic frequency. With a buoyancy profile that decreases with depth, such transport can lead to trapping in the upper ocean as the wave reflects from the ocean surface and lower turning points.

Previous analyses of oceanic observations have described the essential behavior of internal wave propagation in a three-dimensional background flow. Mied et al. (1987, 1990) use ray tracing to depict the rotation and change in magnitude of the horizontal wavevector and evolution of vertical wavenumber for a coherent near-inertial wave packet propagating in a mesoscale eddy field. Joyce and Stalcup (1984) document a high-frequency wave embedded in an upper ocean front. All these studies discuss the departures of the background flow from a state of symmetry [i.e., a parallel shear flow (jet) or azimuthal vortex (ring)]. None provides the succinct summary inherent in the Okubo–Weiss criterion (1) nor makes a distinction between relative vorticity and rate of strain.

In the absence of such a succinct summary, it is easy to appreciate that near-inertial internal wave trapping (Kunze 1985) has provided the conceptual paradigm for internal wave–mean flow interactions. Kunze (1985) argues that the effective lower bound of the internal wave band is not the Coriolis frequency f but rather $f + \zeta/2$, so that near-inertial waves (where near inertial is taken to be near the *effective* Coriolis frequency) located in regions of anticyclonic relative vorticity will have frequencies below f and so will be unable to propagate outside that region.

Near-inertial internal wave trapping was originally motivated by observations (Kunze and Sanford 1984) of large-amplitude, high wavenumber near-inertial waves in an upper ocean frontal regime. Such waves were found to the west of a southward velocity maximum (i.e., in a region of anticyclonic relative vorticity). Kunze (1985) argues that the wave–mean scale separation requirement of the WKB approximation can be relaxed and derives a dispersion relation that, in the limit of small Doppler shifting (wave propagation *across* the frontal jet), can produce the phenomenology of wave trapping. Subsequent detailed studies (Kunze et al. 1995; Kunze and Toole 1997) justifying this characterization have been in symmetric (2D) background flows (a Gulf Stream warm core ring and vortex cap atop a seamount, respectively) in which the observed wave fields had a negligible Doppler shift. In the seamount example, the generation of a subinertial diurnal internal tide was documented. In the warm core ring, the horizontal structure of the wave field was nearly identical to that of the ring, and the presumed source of the observed wave field was inertial pumping associated with mixed layer motions oscillating at the effective Coriolis frequency (Weller 1982).

In a more generic 3D frontal regime or mesoscale eddy field for which (1) applies, it is not clear that near-inertial internal wave trapping is a relevant conceptual paradigm for at least two reasons. First, Doppler shifting will typically make an $O(1)$ contribution to the dispersion relation (Polzin et al. 1996), significantly larger than the $O(R_o = \zeta/f)$ correction that is responsible for trapping nominally subinertial ($f + \zeta/2 \leq \omega \leq f$) internal waves in regions of anticylonic relative vor-

TABLE 1. Environmental parameters and relations derived through linear kinematics for single-plane wave solutions. The subscripts cw and ccw represent the sense of rotation of the velocity vector with depth (Leaman and Sanford 1975): E_{cw} and E_{ccw} are the associated energies; E_k and E_p are kinetic and potential energy; a superscript of the asterisk denotes the complex conjugate of a Fourier coefficient; and $\Re(\phi)$ represents the real part of ϕ. All diagnostics are based on single-plane wave $[e^{i(kx+ly+mz-\sigma t)}]$ solutions to the linearized equations of motion. The hydrostatic approximation has been assumed, and $\bar{\mathbf{u}}$ represents the geostrophic velocity.

Coriolis frequency	f	6.8×10^{-5} s^{-1}
Buoyancy frequency	N	2.4 cph (470–1100 m), 0.78 cph (2100–2730 m)
Eulerian frequency	σ	
Intrinsic frequency	ω	$\sigma - \mathbf{k} \cdot \bar{\mathbf{u}}$
Wavevector	$k = (k, l, m)$	
Horizontal wavenumber	$K_h = (k^2 + l^2)^{1/2}$	
Dispersion relation	K_h/m	$(\omega^2 - f^2)^{1/2}/N$
Energy ratio	$R_{\text{energy}} = E_k/E_p$	$(\omega^2 + f^2)/(\omega^2 - f^2)$
Aspect ratio	$N\,k_h/f\,m$	$[2/(R_{\text{energy}} - 1)]^{1/2}$
Rotary ratio	$R_{\text{rotary}} = E_{cw}/E_{ccw}$	$(\omega + f)^2/(\omega - f)^2$
Group velocity	$\partial\omega/\partial$k	$(N^2/m^2\omega)(k, l)$
Horizontal azimuth (1)	v'^*b'	$\varphi_{v'^*b'} = \tan^{-1}(l\omega/-fk)$
Horizontal azimuth (2)	u'^*b'	$\varphi_{u'^*b'} = \tan^{-1}(k\omega/fl)$
Normal coordinate	θ_n	$\tan(2\theta_n) = 2\Re(u'^*v')/(u'^*u' - v'^*v')$

ticity (Kunze 1985; see the appendix for futher details). Second, a notable loose end is that Kunze's near-inertial wave-trapping scenario requires trapped waves to originate inside regions of anticyclonic relative vorticity. D'Asaro (1995) finds no evidence that near-inertial mixed layer oscillations are refracted by the relative vorticity structure of a weak 3D eddy field. In retrospect, it is obvious that the original interpretation of observations reported in Kunze and Sanford (1984) as an example of near-inertial internal wave trapping should be regarded with caution. That dataset consisted of cross-frontal surveys with no ability to constrain the alongfront phase variations associated with Doppler shifting, and Kunze (1985) develops the idea of near-inertial wave trapping by taking the expedient limit of setting the Doppler shift to zero.

In the following, the MODE data are examined for characteristics of wave propagation relative to the mean flow gradients, and an interpretation is forwarded that they are consistent with the wave-capture scenario rather than representing the background internal wave state or the direct products of atmospheric forcing.

2. The MODE dataset, revisited

The data examined here were obtained as a time series of 28 deployments of an electromagnetic velocity profiler within 20 km of the MODE-1 central mooring (28°N, 69°40′W) during 11−15 June 1973. Leaman and Sanford (1975) and Leaman (1976) report on a subset (20) of these profiles that were obtained directly on top of the central mooring. Sanford (1975) uses these profiles 219–247 to examine the spatial and temporal variability over small horizontal and temporal lags. The following analysis focuses on 37 profiles (of 56 possible up and down traces) having data gaps no larger than three contiguous points. Data gaps have been filled through linear interpolation. The conductivity sensor used in this field program is noisy and, consequently, buoyancy perturbations $b' = g(\rho - \bar{\rho})$ have been estimated with potential temperature (θ) alone. This implicitly assumes a constant temperature–salinity (θ–S) relation. The analysis is thereby restricted to main thermocline (470–1100 m) and abyssal (2100–2730 m) depths. The θ–S relation at these depths is climatologically tight. Uncertainties attributable to this assumption are $O(10\%)$ within the main thermocline and do not affect the interpretation of the results presented here. At intermediate levels influenced by Mediterranean water characteristics, water mass variability precludes buoyancy estimates. Temperature gradient estimates at depths greater than 3000 m are increasingly contaminated by instrumental noise. Diagnostics for this study are provided by relations based on linear internal wave kinematics (Table 1). In the following, $E = E(m)$ is the vertical wavenumber (m) energy spectrum, with subscripts denoting various decompositions.

Prior analysis of these data points out that velocity profiles separated by half an inertial period tend to mirror each other (Fig. 2). Thus, much of the finescale velocity structure is near inertial. In contouring the 5-day time series of velocity profiles, upward-phase propagation is evident (Fig. 3). This implies an excess of downward energy propagation and is consistent with the observed clockwise (cw) rotation with depth of the velocity vector (Leaman and Sanford 1975).

But with the hindsight of 30 years and the personal experience of analyzing thousands of similar profiles,

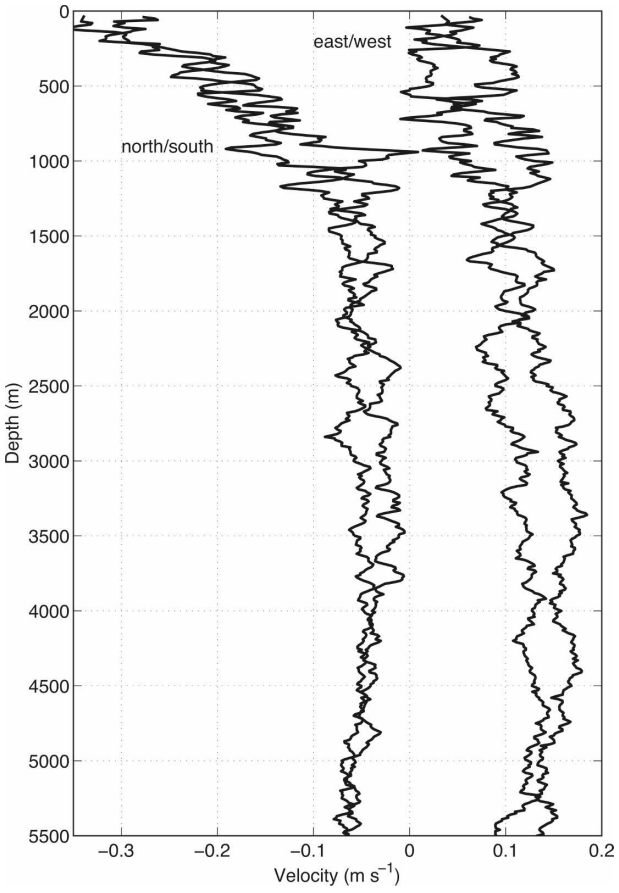

FIG. 2. East and north velocity traces for down profiles 219 and 221, taken 1/2 of an inertial period apart. After Leaman and Sanford (1975), their Fig. 1.

my claim is that data from the thermocline region (500–1000 m) are subtly odd. First, the velocity profile data are not self-similar with depth. The thermocline region appears to have an excess of small-scale energy, which can be quantified with the gradient spectra (Fig. 4). In particular, clockwise ($2m^2\ E_{\rm cw}$) shear is generally enhanced over counterclockwise ($2m^2\ E_{\rm ccw}$) shear and is peaked about wavelengths (λ_v) of 60 m. The excess energy is near inertial in character, and this excess can be quantified through the ratio of horizontal kinetic (E_k) to potential energy (E_p) (Fig. 5). This ratio exhibits a peak coincident with the peak in the cw spectrum. Abyssal spectra are also peaked. That peak occurs at wavenumbers smaller than expected simply on the basis of buoyancy scaling: the WKB approximation implies that vertical wavelengths vary inversely with buoyancy frequency (N), $\lambda_v \propto 1/N$ and the ratio between thermocline and abyssal stratification is a factor of 3.3, smaller than the ratio of the wavenumber peaks. Second, the time-depth series (Fig. 3) reveals the presence of coherent wave packets. The presence of coherent features is not representative of the background wave field. A vertical wavenumber domain coherence analysis between velocity and buoyancy perturbations (Fig. 6) and the two horizontal velocity components (Fig. 7) returns large estimates of coherence at the peak in the shear spectrum; $\lambda_v \cong 60$ m. Coherence estimates are uniformly largest at 64- and 58.2-m vertical wavelengths. In the following, an attempt is made to diagnose wave packet characteristics using amplitude, coherence, and phase estimates at these peak wavenumbers.

a. *Main thermocline wave estimates ($\lambda_v = 64$ and $\lambda_v = 58.2$ m)*

1) ESTIMATES OF WAVE FREQUENCY

One estimate of wave frequency can be obtained from the estimates of velocity–buoyancy phase (Fig. 6; Table 1). The phase estimates exhibit a trend over the range of wavenumbers comprising the packet. Noting, however, that the product of the two phase estimates [$\tan(\varphi_{v'*b'})\ \tan(\varphi_{v'*b'}) = -\omega^2/f^2$ for a single wave] is much more constant than their ratio, the phase estimates at the packet peak are combined to estimate

$$\omega = 1.0 \pm 0.1f,$$

with indicated error representing one standard deviation (Bendat and Piersol 1986).[1]

This frequency estimate is compatible with that obtained by interpreting the observed energy ratio estimates over the same bandwidth as the phase estimates,

$$R_{\rm energy} \equiv \frac{E_k}{E_p} = 12.6,$$

in terms of a single wave:

$$\frac{\omega}{f} = \sqrt{\frac{E_k + E_p}{E_k - E_p}} = 1.08.$$

This second frequency estimate is arguably biased by contributions associated with the background wave field and vortical motions (Polzin et al. 2003). Taking this contribution to be given by the incoherent power,

[1] Uncertainty estimates presented in this work represent random errors assuming Gaussian statistics. Bias errors are possible, e.g., in interpreting the energy ratio $R_{\rm energy}$ as a frequency or aspect ratio characterizing a broadband spectrum, e.g., Polzin et al. (1995). Bias errors are not, in general, reported here because such estimates require making unverifiable assumptions about the statistics of the contaminating field.

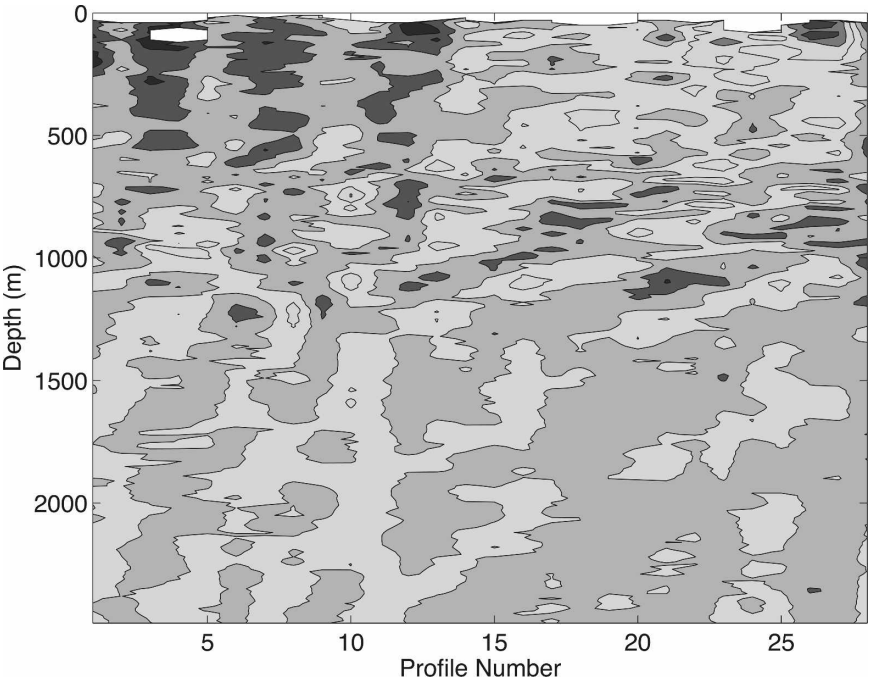

FIG. 3. Contours of eastward velocity during the 5-day time series. The mean profile has been subtracted and resulting profiles have been low-pass filtered to eliminate features having vertical wavelengths larger than 800 m. Only up profiles are used, and the sampling is not precisely uniform in time. Missing data have been interpolated or replaced with the down profile. After Leaman (1976), his Fig. 2.

and attributing this entirely to E_p, an alternate estimate of the wave packet energy ratio is

$$R_{\text{energy}} \equiv \frac{E_k}{E_p} = 18 - 24,$$

with wave frequency

$$\frac{\omega}{f} = \sqrt{\frac{E_k + E_p}{E_k - E_p}} = 1.04 - 1.06.$$

A third frequency estimate is possible using the rotary estimates

$$R_{\text{rotary}} \equiv E_{\text{cw}}/W_{\text{ccw}} = 8.3,$$

for which

$$\frac{\omega}{f} = \frac{\sqrt{R_{\text{rotary}}} + 1}{\sqrt{R_{\text{rotary}}} - 1} = 2.1.$$

The implication here is that there is a significant contamination to the single-wave interpretation of the rotary diagnostic. If $\omega = 1.08f$, the single-wave rotary ratio is 676. Nonlinearity can provide a rational for reduced rotary ratios at near-inertial frequencies.

In the cascade representation of nonlinearity described in Polzin (2004), momentum conservation is obtained by backscattering into an oppositely signed wavevector at a rate proportional to the downscale energy cascade. For a boundary source, this closure scheme returns a peak in the ratio of upward- and downward-propagating wave spectra at wavenumbers a factor of 2 to 3 smaller than that defined by $2\int_0^{m_c} m^2 E_k dm = 0.7N^2$. In the background wave field, $m_c = 0.1$ cpm. The peak in cw/ccw spectral ratio occurs at wavenumber $m_p = 1/58.2$ m^{-1}, for which the shear variance is $2\int_0^{m_p} m^2 E_k dm = 0.32N^2$. Interpreting rotary ratio as being significantly contaminated and rejecting the rotary estimate of wave frequency is consistent with that closure scheme.

A fourth estimate is that of Eulerian frequency. Assuming a single-plane wave solution, wave phase (φ) is given by the linear relation

$$\varphi = mz - \sigma t, \tag{4}$$

so that with positive σ, wave crests (lines of constant phase) propagate upward if $m > 0$. Here, the Fourier transform is used to isolate the packet wavelength over the transform interval so that the term mz in (4) is

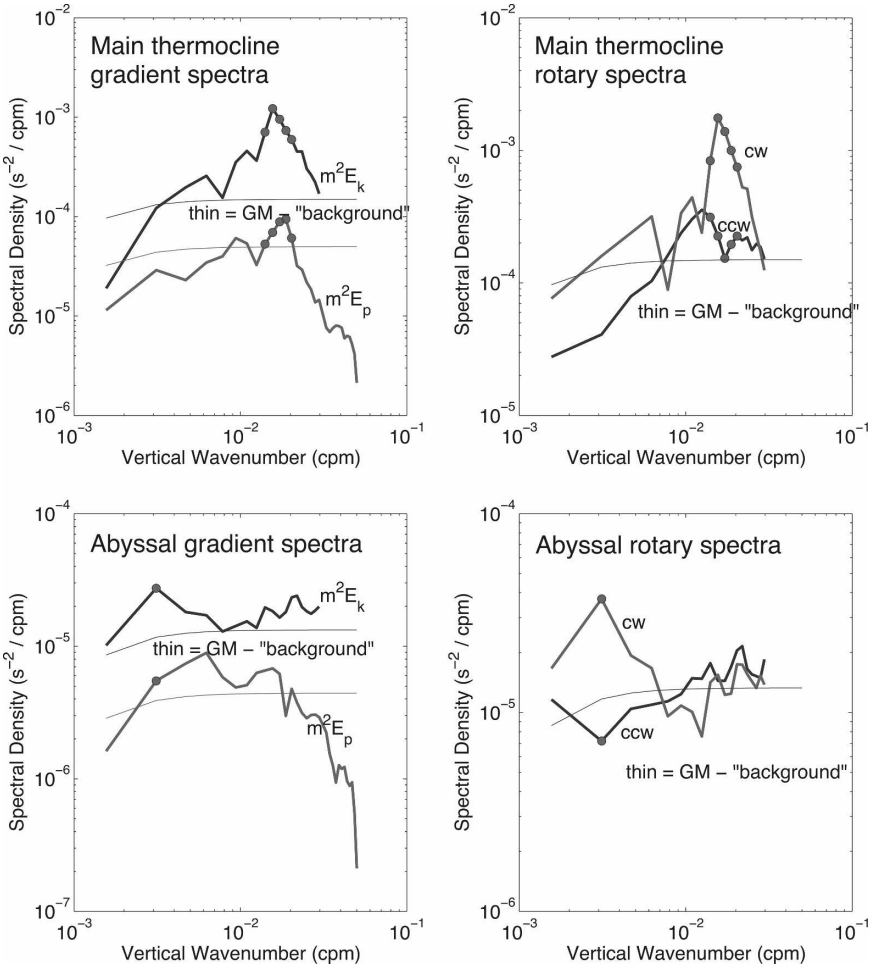

FIG. 4. (top) Main thermocline and (bottom) abyssal (left) gradient spectra and (right) rotary spectra. The thin lines represent spectral levels associated with the isotropic GM76 (Cairns and Williams 1976) model. Spectra were estimated from 37 (of 56 possible) profiles having data gaps smaller than 4 points. Main thermocline spectra were estimated over depths of 470–1100 m, abyssal spectra 2100–2730 m. Filled circles are used to represent wave packets. (See text for details.)

effectively constant. The rotary decomposition effectively isolates upward- and downward-phase propagation for near-inertial waves, so that the time rate of change of observed cw Fourier coefficient phase (Fig. 8) provides an estimate of the wave packet's Eulerian frequency. Linear regression of phase against time returns

$$\sigma = 4.4 \pm 0.15 \times 10^{-5}\mathrm{s}^{-1},$$

with the quoted uncertainty representing one standard error. The estimate is subinertial ($f = 6.8 \times 10^{-5}$ s^{-1}) and linear internal wave kinematics (i.e., a superinertial intrinsic frequency) require significant Doppler shifting of a northward-propagating wave.

2) HORIZONTAL WAVENUMBER AZIMUTH ESTIMATES

Using the linear diagnostic $\tan(\varphi_{v'*b'})/(\varphi_{u'*b'}) = k^2/-l^2$, estimates of velocity–buoyancy–phase return, with one standard deviation uncertainty,

$$\frac{|k|}{|l|}(\lambda_v = 64\ \mathrm{m}, \lambda_v = 58.2\ \mathrm{m}) = [1.09(0.95 - 1.25), 1.99(1.69 - 2.34)].$$

Phase propagation of this wave is to the north and west, in addition to being upward.

The linear diagnostic for the orientation of the major axis of the current ellipse (Table 1) returns

$$\theta_n(\lambda_v = 64\ \mathrm{m}, \lambda_v = 58.2\ \mathrm{m}) = (0.97, 0.64)\,\mathrm{rad}.$$

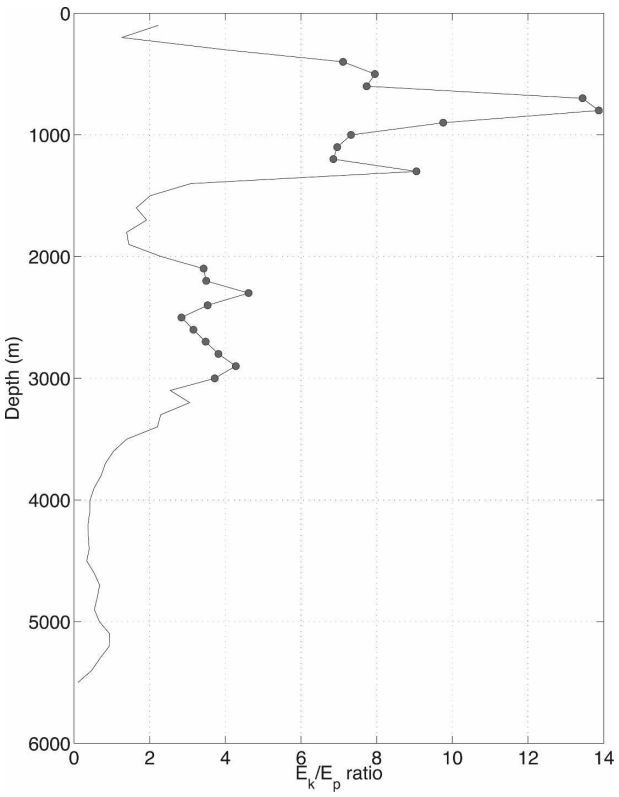

FIG. 5. Energy ratio E_k/E_p estimates formed from 10-m first differences. Larger values imply lower frequency (see Table 1). Due to instrument noise in the CTD and water mass variability, I only trust data represented as filled circles.

With $(k, l) = k_h[\cos(\theta_n), \sin(\theta_n)]$,

$$\frac{|k|}{|l|}(\lambda_v = 64 \text{ m}, \lambda_v = 58.2 \text{ m}) = (0.69, 1.34).$$

The trend of the wavevector's horizontal azimuth with increasing vertical wavenumber estimated from the orientation of the major axis of the horizontal current ellipse is consistent with the horizontal azimuth estimated from the velocity–buoyancy phase. The mean, however, differs. The major axis estimate of the horizontal azimuth (θ_n) is regarded as being less reliable than that associated with the velocity–buoyancy phase because of possible subtractive cancellation in the denominator of the normal coordinate definition (Table 1). Consequently, the velocity–buoyancy phase estimates of horizontal azimuth are used below.

The dispersion relation provides an estimate of horizontal wavenumber magnitude [$k_h = \pm m(\omega^2 - f^2)^{1/2}N$], and thus with $|k|/|l| = 1.5$ and $\omega = 1.08f$:

$$(k, l) = (-2\pi/11, 2\pi/17)\text{km}^{-1}.$$

3) WAVE–MEAN INTERACTIONS

Further insight can be gained by interpreting the data in the context of the geostrophic flow field. The mean baroclinic shear profile (Fig. 9) indicates southward, surface- intensified flow. The MODE central current meter at nominally 3000-m depth indicates a mean current of $(\bar{u}, \bar{v}) = (5.8, 2.8)$ cm s^{-1} over the time period of the profiler dataset, so that only minor adjustments to the baroclinic profile from the electromagnetic velocity profiler (EMVP; Fig. 9) are required to render the velocity estimates absolute. The Doppler shift associated with advection by the mean field is significant,

$$-l\bar{V} \cong \frac{2\pi}{17\text{km}} 0.07 \text{ m s}^{-1} = 2.6 \times 10^{-5} \text{ s}^{-1},$$

relative to $f = 6.8 \times 10^{-5}$ s^{-1} and makes an $O(1)$ contribution in the dispersion relation. Advection by the mean flow at the level of the transform interval, $(\bar{u}, \bar{v}) = (0, -7)$ cm s^{-1}, dominates the rate at which the coherent features can propagate through: $\mathbf{C}_g = (-1.3, 0.8)$ cm s^{-1}. The Eulerian frequency and Doppler shift estimates

$$\sigma - l\bar{V} = 4.4 \pm 0.15 \times 10^{-5} \text{ s}^{-1} + 2.6 \pm 0.4 \times 10^{-5} \text{ s}^{-1} = (1.03 \pm 0.07)f$$

provide an intrinsic frequency estimate consistent with that derived from the energy ratio, $\omega = 1.08f = 7.3 \times 10^{-5}\text{s}^{-1}$. With horizontal-phase propagation to the northwest and downward energy propagation in a southward jet, the coherent features are propagating in thermal wind shear with increasing vertical wavenumber $dm/dt = -l\bar{v}_z > 0$.

Having ascertained the importance of Doppler shifting and thermal wind shear for the vertical evolution of the thermocline wave packet, the remaining question is the role of the horizontal gradients. Maps of the geostrophic streamfunction (McWilliams 1976; Lee and Wunsch 1977) indicate a straining feature immediately to the north of the experimental site (Fig. 10). In the analysis of Bühler and McIntyre (2005) and Jones (1969), this strain will preferentially orient wave fronts, cascade wave phase to higher horizontal wavenumbers, and act as a funnel in advecting high wavenumber, low intrinsic frequency waves southward. On the other hand, the same map could be cited to support the significance of relative vorticity at the time and location of the observations.

One proposed role of relative vorticity is near-inertial wave trapping. Kunze (1985) advocates the use of

$$\omega \cong f + \zeta/2 + \frac{N^2k_h^2}{2fm^2} + \frac{1}{m}(l\bar{u}_z - k\bar{v}_z)$$

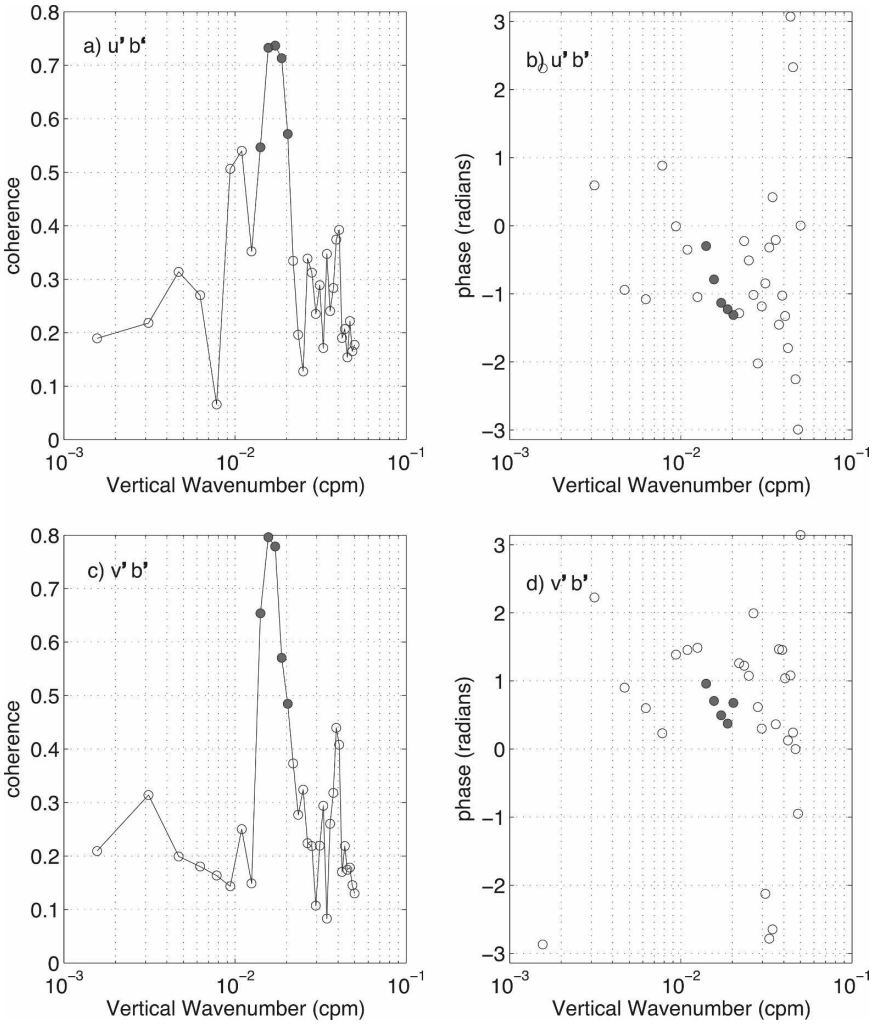

FIG. 6. Main thermocline velocity–buoyancy coherence (a) $[u'b']$, (c) $[v'b']$ and phase (b) $[u'b']$, (d) $[v'b']$ estimates. Filled circles denote the wave packet bandwidth.

rather than the more conventional

$$\omega = \left(\frac{N^2 k_h^2 + f^2 m^2}{m^2} \right)^{1/2}.$$

Estimating relative vorticity $\zeta = \bar{v}_x - \bar{u}_y$ magnitude as $\zeta \cong \bar{v} = \bar{v}_x / L$, with $\bar{v} = -0.07$ m s^{-1} taken as the average velocity in the absolute profile (Fig. 9) over the transform interval and length scale $L = 100$ km taken from the geostrophic streamfunction map (Fig. 10), the contribution of relative vorticity to the proposed dispersion relation is nearly two orders of magnitude smaller than intrinsic, Eulerian, or Coriolis frequencies. The term representing buoyancy forces is an order of magnitude larger. Consequently, I am led to the inference that the dynamics in this three-dimensional system are dictated by variations in the Doppler shift rather than by variations in relative vorticity.

A second proposed role is through (1). Averaged over daily intervals, southward thermocline shear exhibits neither a decreasing nor an increasing trend and suggests that with the observed westward drift of the southward jet (Lee and Wunsch 1977), the observations were obtained near the velocity maximum of the southward jet. The velocity maximum represents a region of sign transition for the relative vorticity and implies that strain locally dominates vorticity. However, it is not simply the local conditions that dictate the wave packet's characteristics.

In the context of a ray-tracing analysis, the observed packet characteristics represent the time history of wave–mean interactions along the ray path. For near-inertial waves with a horizontal group velocity that is small relative to the background velocity, the ray trajectories are clearly dominated by horizontal advection.

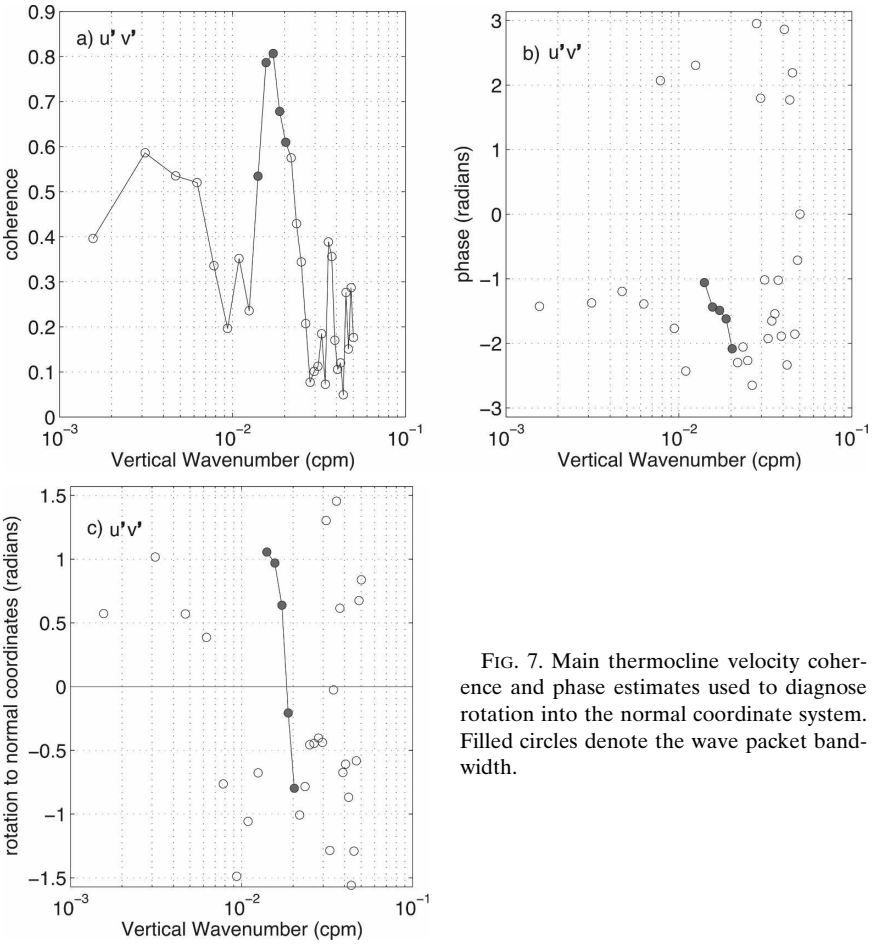

FIG. 7. Main thermocline velocity coherence and phase estimates used to diagnose rotation into the normal coordinate system. Filled circles denote the wave packet bandwidth.

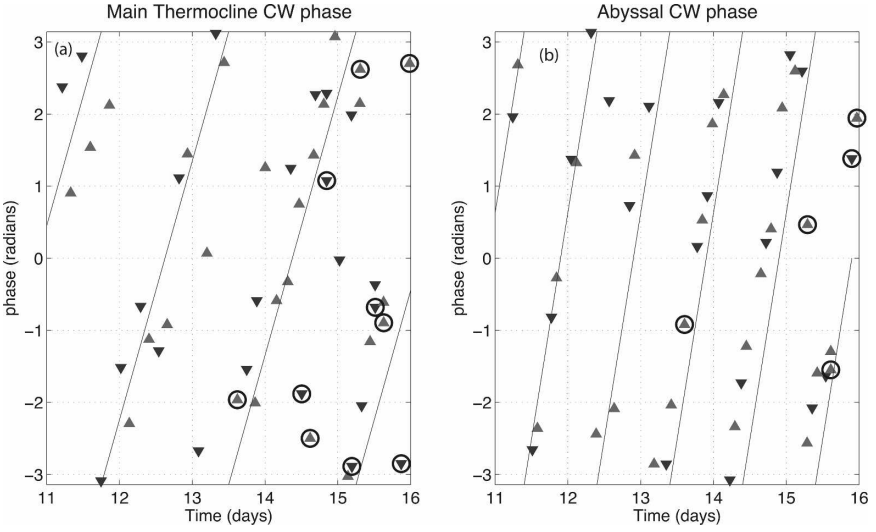

FIG. 8. Rotary (cw) phase estimates for (a) main thermocline and (b) abyssal depth intervals. Inverted triangles represent data obtained profiling downward, normal triangles represent the upward traces, and circles are drawn around those phase estimates from deployments spatially removed from MODE center. The thin line represents the phase progression of an upward-propagating wave with Eulerian period of (a) 1.75 and (b) 1.00 days. The time axis is the month/day of June 1973.

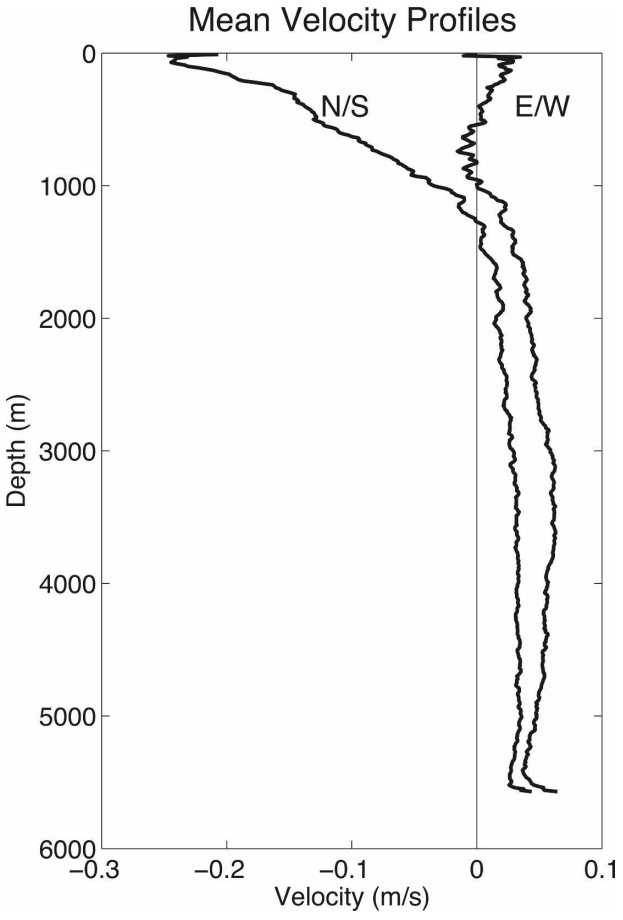

FIG. 9. Mean profiles of baroclinic velocity from EMVP, rendered absolute by matching with the 5-day mean current estimated at a nearby moored current meter at 3000-m depth.

It is a straightforward matter to summarize the streamfunction (Fig. 10) with an analytic representation and to back trace internal waves through it.[2] It is more involved, but still possible, to estimate the geostrophic streamfunction with a time-dependent objective mapping procedure and back trace rays through that field. Experience with the analytic representations suggest that because the system is dominated by horizontal advection, it is a trivial matter to select initial conditions that are not statistically different from the observed wave characteristics that have ray trajectories leading back to where the rate of strain variance obviously exceeds the vorticity variance. But without observations of the spatial–temporal evolution of the wave packet, neither exercise proves anything other than that the observations are plausibly consistent with the dynamics being dominated by variations in Doppler shifting.

Asymptotically, the combination of horizontal straining and propagation in vertical shear will produce a wave aspect ratio of (Bühler and McIntyre 2005)

$$\frac{fm}{Nk_h} = \frac{f}{Nk_h}\frac{-\mathbf{k}\cdot\bar{\mathbf{u}}_z}{\sqrt{D}} \cong \frac{-l\bar{v}_z/N}{k_h\sqrt{D}/f} \leq \frac{\bar{v}_z/N}{\sqrt{D}/f} = 3.3,$$

with $\bar{v}_z = -2.4 \times 10^{-4}\text{s}^{-1}$ and $\sqrt{D} \cong \bar{v}_y = \bar{v}/L$, with $\bar{v} = -0.07$ m s^{-1} taken as averages from the absolute velocity profile (Fig. 9) over the transform interval and length scale $L = 60$ km taken from the geostrophic streamfunction map (Fig. 10). Predicted energy ratios are

$$\frac{E_k}{E_p} = 2 \times \left(\frac{fm}{Nk_h}\right)^2 + 1 \leq 23,$$

which are significantly larger than either the observations (12.6) or those associated with the Garrett and Munk (1975) models, for which $E_k/E_p = 3$. Note that maxima in vertical shear and horizontal strain are likely *not* collocated, so that $\bar{v}_z/\sqrt{D}$ varies over the advective time scale $\bar{v}/L \cong \sqrt{D}$, and that the estimated zonal group velocity is similar to the observed westward drift of the mesoscale eddy field. These are conditions not considered in the asymptotic result (2). Similarly, one could argue for either smaller values of $\sqrt{D}$ associated with possible cancellation of strain variance and relative vorticity variance at the observational site or larger effective values of $\sqrt{D}$ associated with nonlocal conditions as the downward-propagating wave will have experienced larger typical horizontal velocities than $\bar{v} = 0.07$ m s^{-1} along the ray trajectory from the upper ocean.

I simply conclude that the MODE thermocline data are consistent with the dynamics being dominated by variations in Doppler shifting, of which wave capture is an asymptotic expression. Those asymptotics, $m\sqrt{D} = -\mathbf{k}\cdot\bar{\mathbf{u}}_z$ (2), provide an upper bound to wave aspect ratio m/k_h (3) and a lower bound to the intrinsic frequency w that are consistent with the observations.

b. *Abyssal wave estimates [$\lambda_v = 320$ m]*

The abyssal wave signatures (Figs. 11 and 12) are more difficult to characterize, in part because the wave packet at $\lambda_v = 320$ m does not stand out as strongly from the background and also because of lower signal-to-instrumental noise ratios. Whatever the cause, ve-

[2] Try, e.g., $\psi(x, y, z, t) = \psi_o \sin(Kx - \Omega t)\sin(Ly)\cos(Mz)$ with $(\bar{u}, \bar{v}) = (\psi_y, -\psi_x)$, $= -\beta K/[K^2 + L^2 + (fM/N)^2]$, $\beta = 2 \times 10^{-11}$ m^{-1} s^{-1}, M representing the first baroclinic mode in a 2000-m-deep ocean, $f = 6.8 \times 10^{-5}$ s^{-1}, $N = 4.2 \times 10^{-3}$ s^{-1}, $K = L = 2\pi/360$ km^{-1}, and ψ_o is taken to be maximum velocities of 0.25 m s^{-1}, $\psi_o = 0.25/\sqrt{K^2 + L^2}$ m^{2}s^{-1} and initial position $x(t = 0) = [x = 0, y = -90$ km, $z = 1100$ m (above bottom)].

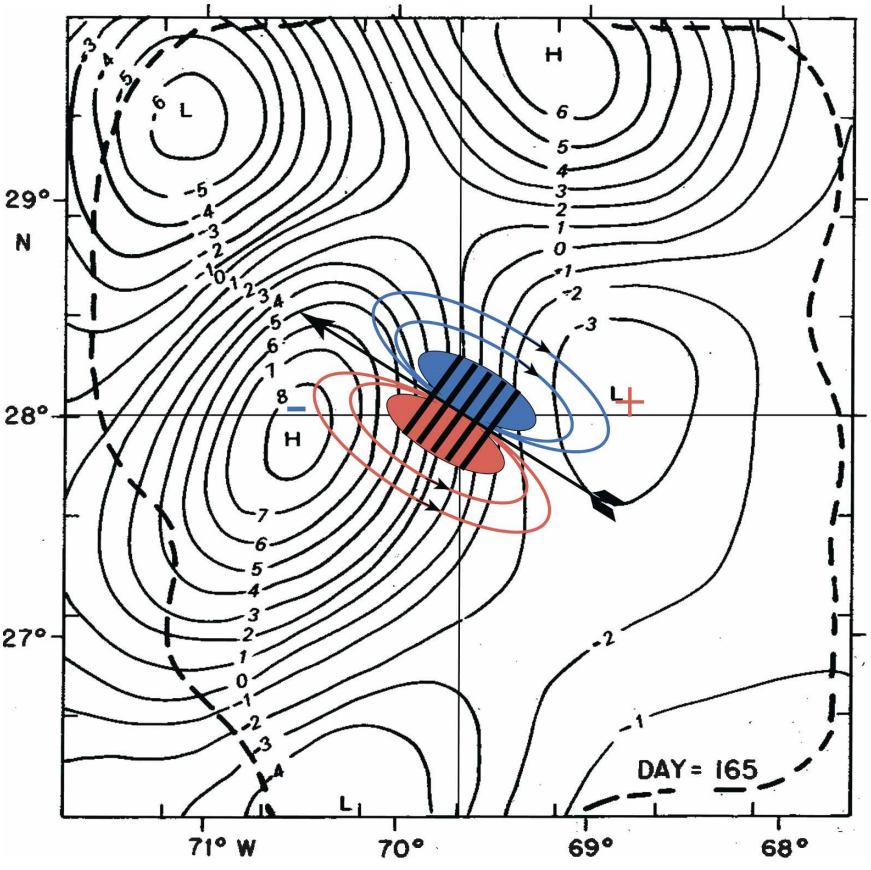

FIG. 10. A map of the 500-m geostrophic streamfunction (McWilliams 1976; Lee and Wunsch 1977) from MODE, day 165, 1973 (14 Jun, ± 3 days), with a schematic depiction of wave crests (thick solid lines at approximately one horizontal wavelength separation) and wavevector (the arrow) associated with the coherent features noted in data reported by Sanford (1975) and Leaman and Sanford (1975) and reanalyzed here. The streamfunction map indicates a straining feature immediately to the north of the experimental site (28°N, 69°40′W, with data taken over 11–15 Jun, a time frame that includes day 165). In the shrinking catastrophe and wave capture scenarios, this strain will preferentially orient wave fronts and cascade wave phase to higher horizontal wavenumber. The orientation of the wave phase in the horizontal and vertical is consistent with the Bühler and McIntyre (2005) wave-capture scenario for a wave propagating downward in the southward surface-intensified jet. Also depicted is the dipole structure (Bühler and McIntyre 2005) associated with the wave packet and its circulation. Note that this vorticity signature opposes that associated with the mesoscale field: potential vorticity contours differ from the geostrophic streamfunction contours only in the advection of relative vorticity (McWilliams 1976). High and low pressure centers are associated with negative and positive relative vorticity, respectively. Bühler and McIntyre (2005) forward the hypothesis that the dipole becomes locked into the mean flow as the internal wave dissipates. Thus, wave capture provides a mechanism for mixing potential vorticity.

locity–buoyancy coherence is not statistically different from zero (Fig. 11). The restricted set of diagnostics are

$$R_{\text{energy}} \equiv \frac{E_k}{E_p} = 5.0,$$

$$R_{\text{rotary}} \equiv E_{\text{cw}}/E_{\text{ccw}} = 5.2,$$

$$\theta_n = 1.20 \text{ rad},$$

$$\sigma = 7.70 \pm 0.08 \times 10^{-5}\text{s}^{-1} = (1.13 \pm 0.01)f.$$

The major axis lies in the north-northwest/south-southeast direction.

Taking these estimates at face value and interpreting them in terms of a single wave yields

$$\frac{\omega}{f} = \sqrt{\frac{E_k + E_p}{E_k - E_p}} = 1.22,$$

$$\frac{|k|}{|l|}(\lambda_v = 320 \text{ m}) = 0.39.$$

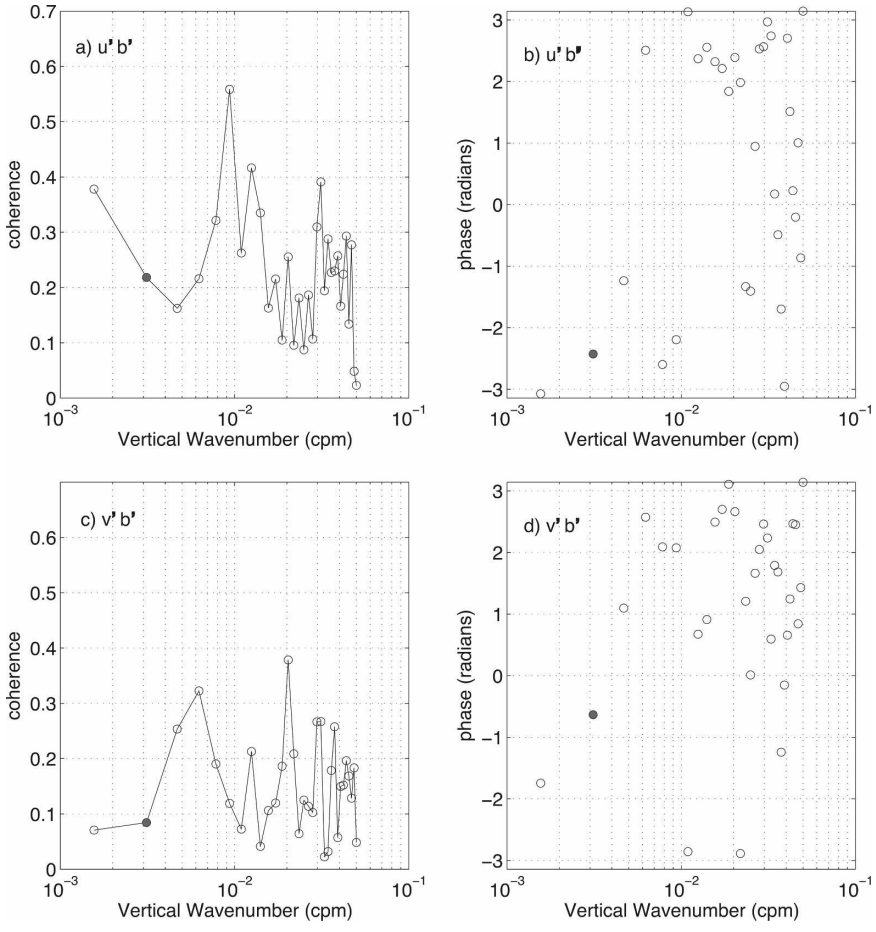

FIG. 11. Abyssal velocity–buoyancy coherence (a) $[u'b']$, (c) $[v'b']$ and phase (b) $[u'b']$, (d) $[v'b']$ estimates. Filled circles denote the wave packet bandwidth.

Assuming propagation to the northwest,

$$(k, l) = (-2\pi/25, 2\pi/9.8)\ \mathrm{km}^{-1}.$$

Advection by the mean flow $(\bar{u}, \bar{v}) = (4.7, 2.1)\ \mathrm{cm\ s}^{-1}$ is difficult to distinguish in magnitude from the nominal group velocity $\mathbf{C}_g = (-1.5,\ 3.7)\ \mathrm{cm\ s}^{-1}$ associated with the coherent features. Doppler shifting,

$$-k\bar{v} - l\bar{v} \cong \frac{2\pi}{25\ \mathrm{km}}\,0.047\ \mathrm{m\ s}^{-1} - \frac{2\pi}{9.8\ \mathrm{km}}\,0.021\ \mathrm{m\ s}^{-1}$$

$$= 1.2 \times 10^{-5}\ \mathrm{s}^{-1} - 1.3 \times 10^{-5}\ \mathrm{s}^{-1},$$

is not significantly different from zero, indicating that wave crests are aligned with the streamlines. The flow field at these depths is directed slightly north of east (Lee and Wunsch 1977) rather than southward as noted in the thermocline.

The Eulerian frequencies in the abyss and thermocline are significantly different, with the implication that the excess of E_{cw} throughout the water column is not associated with a single wave encountering a depth-varying Doppler shift.

3. Summary and discussion

The dataset of velocity and temperature profiles obtained by Sanford during MODE (Sanford 1975; Leaman and Sanford 1975; Leaman 1976) contains a near-inertial wave packet in the main thermocline with a vertical wavelength of 60 m and a wavevector directed upward and to the northwest. Ratios of horizontal kinetic to potential energy are significantly larger in the main thermocline than at middepth or specified through the Garrett and Munk models. The large ratios indicate greater near-inertial energy and are dominated by contributions from the wave packet. Despite these observations providing the basis for a revision to the Garrett and Munk empirical description of the background wave field (Garrett and Munk 1975), the presence of the wave packet and anomalous characteristics

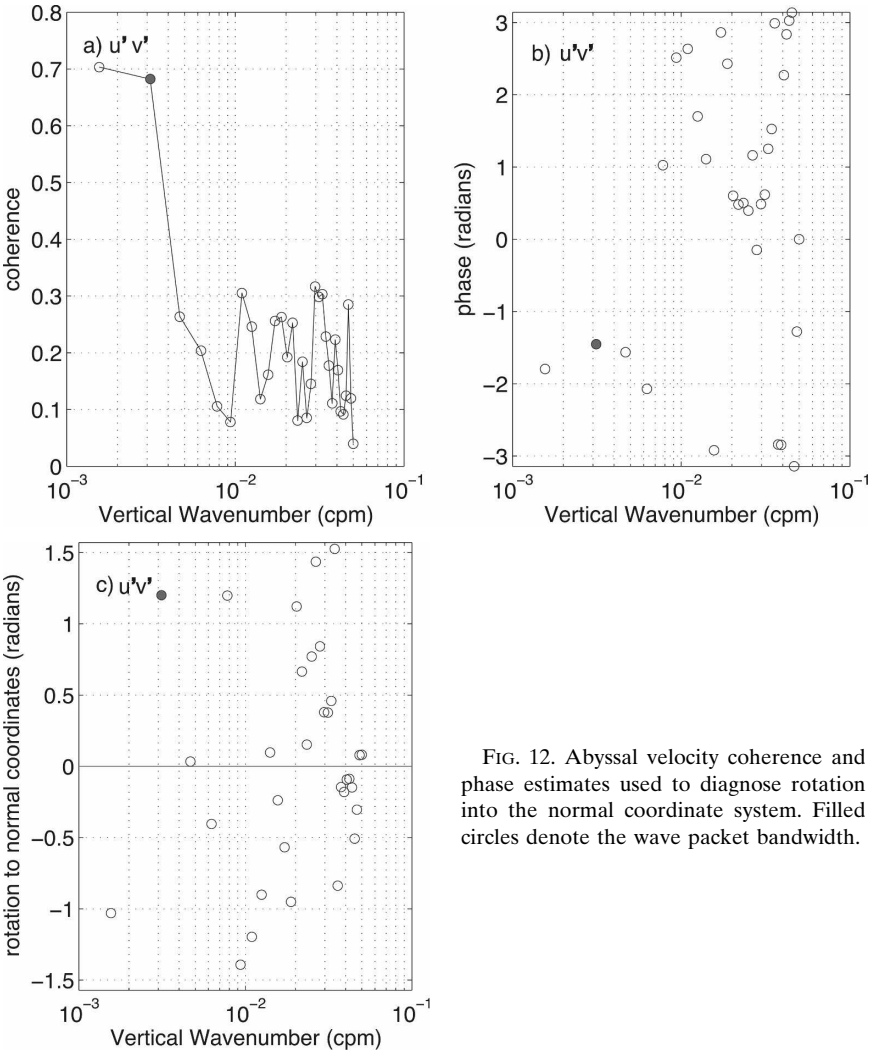

FIG. 12. Abyssal velocity coherence and phase estimates used to diagnose rotation into the normal coordinate system. Filled circles denote the wave packet bandwidth.

at a high vertical wavenumber are not consistent with the dataset representing the background wave field. Moreover, the wave packet is not likely to be the direct by-product of atmospheric generation (Leaman 1976) as its vertical group velocity places it some 80 days away from the surface, comparable to the dissipation time scale for the entire background internal wave field. A near-inertial wave having the observed vertical wavelength and amplitude would likely dissipate over a much shorter time scale. The MODE thermocline data are consistent with the dynamics being dominated by variations in Doppler shifting. Near-inertial wave trapping (Kunze 1985), for which Doppler shifting is assumed to be negligible, is not an appropriate characterization of wave–mean interaction in this 3D background field.

Doppler shifting of the wave packet is significant and the vertical wavenumber magnitude is increasing as the wave propagates in thermal wind shear at the base of the thermocline. Bühler and McIntyre (2005) argue that the problem of small-amplitude waves interacting with a larger-scale 3D flow field only through Doppler shifting is kinematically similar to the issue of particle pair separation. If the background strain variance dominates the background vorticity variance, the ray equations lead to an exponential increase/decrease in horizontal *wavenumber*. Vorticity simply tends to rotate the horizontal *wavevector* in physical space. In this 3D problem, the vertical wavenumber is slaved to the horizontal, so that exponential growth of the horizontal wavenumber implies either exponential growth or decay of the vertical wavenumber in the presence of thermal wind shear. Those waves with growing horizontal and vertical wavenumber magnitude will tend to be captured within the extensive elements of the eddy strain field and eventually dissipate: an extensive element acts as a funnel to collect high wavenumber, low intrinsic frequency waves. Estimates of the geostrophic

streamfunction (McWilliams 1976) place the observations within an extensive element of the mesoscale strain field.

The above summary addresses the quantitative results from the analysis of this dataset. The implications are much broader in scope.

First, the wave-capture dynamic described above is essentially that invoked by Müller (1976) in a much more sophisticated treatment of a radiation balance equation. That approach enables calculation of the rate at which energy and momentum are transferred from the mesoscale eddy field to the internal wave field. That model treats mesoscale eddies as a three-dimensional field, and permanent transfer is associated with wave dissipation, but one's notion of "dissipation" needs to include the irreversible effects of weak nonlinearity acting on the internal wave field. With this expanded notion and, if the ability of internal wave packets to escape capture are accounted for, Müller's model can be manipulated to make sensible predictions for the observed transfer rates (P0b).

Second, the bulk of the literature regarding internal wave–mean flow interactions focuses on symmetric (2D) flows, but the consequences of assuming symmetric background states are virtually unappreciated. The introduction of symmetry in the case of parallel shear flows (Jones 1967) or circular vortices (Ooyama 1966) greatly simplifies the analysis. But it comes at a cost. In a zonal flow, the flux of zonal angular pseudomomentum ($\mathbf{C}_g k\mathcal{A}$) is nondivergent. For a circular vortex, the flux of azimuthal pseudomomentum is nondivergent. This constraint is usually referred to as Andrews and McIntyre's generalized Eliassen–Palm flux theorem:

$$\frac{dk\mathcal{A}}{dt} + \boldsymbol{\nabla} \cdot \mathbf{F} = \mathcal{D} + O(\alpha^3), \tag{5}$$

which states that in the absence of dissipation $\mathcal{D}$ and nonlinearity (small wave amplitude α limit), and for steady conditions, the pseudomomentum flux $\mathbf{F}$ is spatially nondivergent. In the ray-tracing limit, $\mathbf{F} = k\mathbf{C}_g\mathcal{A}$ and the streamwise (zonal) wavenumber k is constant, so that the Eliassen–Palm flux theorem is nothing more than an action flux conservation statement.

What is not immediately obvious is that the generalized Eliassen–Palm flux theorem does *not* apply to asymmetric (3D) flows. With action conservation and variation of the streamwise wavenumber, the pseudomomentum flux is not conserved. A simple rationalization of the difference in behavior between 2D and 3D systems comes from theoretical physics: each symmetry exhibited by a Hamiltonian system corresponds to a conservation principle [Nöther's theorem, e.g., Sheppard (1990)]. For spatial symmetries the conservation principle concerns momentum: axisymmetric flows preserve the flux of pseudomomentum in the symmetric coordinate. The straining of waves provides the essential mechanism through which the streamwise wavenumber varies, and streamwise pseudomomentum is not conserved.

Third, there are profound consequences for pseudomomentum and vorticity originally described in a nonrotating context by Bretherton (1969) and considered more fully in Bühler and McIntyre (2005). The momentum flux associated with a plane internal wave of infinite spatial extent is nondivergent and that plane wave has no potential vorticity signature. However, a wave packet of finite extent in *both* horizontal directions will have a momentum flux divergence associated with its envelope structure, which in turn induces accelerations on the packet scale, resulting in a dipole vortex structure. In a 3D system, pseudomomentum is not conserved following wave–mean interactions, and Bühler and McIntyre (2005) argue that with modulation of the wave pseudomomentum are modulations in the potential vorticity signature of the wave packet. The modulation of wave pseudomomentum by mesoscale eddy strain is especially significant because it provides a mechanism for damping potential vorticity anomalies associated with the mesoscale eddy field: the wave packet undergoing capture has a vorticity signature that opposes the vorticity distribution in the eddy field (Fig. 10). Dissipation of the captured wave implies a permanent mixing of potential vorticity. Companion manuscripts (P0a,b) explore these issues using data from the PolyMode experiment.

This trading of wave pseudomomentum for eddy potential vorticity is a characteristic of waves interacting with a 3D background. It does not occur within a 2D (symmetric) background. Thus for the purpose of this paper, a mesoscale eddy is *not* an axisymmetric vortex or jet. The pertinent quantity is a nonzero rate of strain, and on this ground, a linear Rossby wave field qualifies.

Finally, the Okubo–Weiss criterion (1) is a generic description of wave–mean interactions when the mean is an asymmetric nondivergent flow. This characterization (1) comes about simply through the Doppler shift and is independent of the character of the dispersion relation. In particular, it carries over to the interaction of Rossby waves with the general circulation and may be a key feature of upgradient potential vorticity transfers and/or recirculation gyre dynamics. There is a crucial distinction, though, between internal waves and planetary wave kinematics regarding coupling with the background horizontal gradients. For internal waves, the horizontal velocity trace is parallel to the projection

of the wavevector onto the horizontal axis. Consequently, an internal wave undergoing capture will gain energy as it does work on the background. For planetary waves, geostrophy dictates that the horizontal velocity trace is perpendicular to the horizontal wavevector. Consequently, a planetary wave undergoing capture will lose energy as it interacts with the background. If parametrically represented through a flux-gradient relation, the internal wave case implies a *positive* horizontal eddy viscosity and the planetary wave case implies a *negative* horizontal eddy viscosity. Bryden (1982) presents estimates of energy exchanges between the mesoscale eddy and time–mean fields in the southern recirculation gyre of the Gulf Stream that are consistent with a negative eddy viscosity acting on a 3D flow field. Brown and Owens (1981) present estimates of energy exchanges between the internal wave field and mesoscale eddy field that are consistent with a positive eddy viscosity acting on a 3D flow field. The internal wave and mesoscale eddy energy and enstrophy (potential vorticity squared) budgets within the southern recirculation gyre are reexamined in P0b.

In summary, my hypothesis is that the bandwidth-limited, coherent features in this dataset are a product of the horizontal strain and vertical shear within the geostrophic flow field.

Acknowledgments. I am indebted to Tom Sanford for his assistance in making this investigation possible. In forwarding this interpretation, I am cognizant of being afforded the luxury of hindsight. The motivation for pursuing reanalysis of the MODE data is not to refute the prior analysis. Thirty years' worth of communal research and personal experience analyzing many similar datasets provide a much more substantial backdrop against which to appreciate the idiosyncrasies of this particular dataset. The motivation is the historical context of this dataset, and an appreciation that answers to some very profound and fundamental questions about rotating stratified fluids have been in sight for more than three decades.

I thank M. McIntyre for forwarding a preprint of Bühler and McIntyre (2005) and subsequent discussions about the topic. Salary support for this analysis was provided by Woods Hole Oceanographic Institution bridge support funds.

APPENDIX

Wave–Mean Interactions in the Ray-Tracing Paradigm

Consider trying to describe the interaction of internal waves and mesoscale eddies through a self-consistent expansion of the equations of motion. Such a derivation starts by invoking a decomposition of velocity [$\mathbf{u} = (u, v, w)$], buoyancy ($b = -g\rho/\rho_o$ with gravitational constant g and density ρ), and pressure (π) fields into "mean" ($-$) and small-amplitude internal wave ($'$) perturbations on the basis of a time-scale separation: $\phi = \overline{\phi} + \phi'$ with $\overline{\phi} = \tau^{-1}\int_0^\tau \phi\, dt$ in which τ is much longer than the internal wave time scale but smaller than the eddy time scale. Progress depends on deriving a wave equation and seeking approximate solutions to that equation.

a. Asymmetric (3D) background fields

For 3D [$\overline{\phi} = \overline{\phi}(x, y, z)$] background fields, it is not possible to manipulate the linearized equations of motion into a wave equation without invoking the small Rossby number [$R_o = \zeta/f = (\bar{v}_x - \bar{u}_y)/f \ll 1$], Froude number [$F_r = (\bar{u}_z^2 + \bar{v}_z^2)^{1/2}/N \ll 1$] limits and invoking a scale separation between the background and wave field. This is the ray-tracing paradigm with locally valid plane wave solutions {i.e., all wave variables are assumed to be proportional to $\exp[i(\mathbf{k}\cdot\mathbf{x} - \sigma t)]$ with wavenumber $\mathbf{k} = (k, l, m)$, horizontal wavenumber magnitude $k_h = (k^2 + l^2)^{1/2}$, and Eulerian frequency σ}.

Ray tracing implies continuity of a real-valued phase function $\Omega = \omega + \mathbf{k}\cdot\mathbf{u}$, with intrinsic frequency given by a dispersion relation. Here the dispersion relation is $\omega^2 = (N^2k_h^2 + f^2m^2)/m^2$. Ray tracing also implies conservation of wave action, $\mathcal{A} = E/\omega$, so that for steady conditions in the absence of nonlinearity and dissipation the action flux is nondivergent:

$$\nabla\cdot(\overline{\mathbf{u}} + \mathbf{C}_g)\mathcal{A} = 0. \tag{A1}$$

The evolution of the wavevector following the wave packet is given by the spatial gradient (denoted by ∇) of the phase function:

$$\frac{d\mathrm{k}}{dt} = -\nabla\Omega. \tag{A2}$$

Componentwise for the wavevector evolution,

$$\begin{aligned}
\frac{dk}{dt} &= -k\bar{u}_x - l\bar{v}_x - m\bar{w}_x,\\
\frac{dl}{dt} &= -k\bar{u}_y - l\bar{v}_y - m\bar{w}_y,\\
\frac{dm}{dt} &= -k\bar{u}_z - l\bar{v}_z - m\bar{w}_z.
\end{aligned} \tag{A3}$$

Consistent with the slowly varying approximation, the velocity gradients are viewed as constant along ray paths and (A3) represents a system of linear first-order constant coefficient differential equations. Assuming

that k $\propto e^{\alpha t}$, the system (A3) can be reduced to a cubic equation for α:

$$\alpha^3 + \alpha[\overline{u}_x\overline{v}_y - \overline{v}_x\overline{u}_y + \overline{w}_z(\overline{u}_x + \overline{v}_y) - (\overline{w}_y\overline{v}_z + \overline{w}_x\overline{u}_z)] + \overline{w}_z(\overline{u}_x\overline{v}_y - \overline{v}_x\overline{u}_y) + \overline{w}_y(\overline{v}_x\overline{u}_z - \overline{u}_x\overline{v}_z) + \overline{w}_x(\overline{u}_y\overline{v}_z - \overline{v}_y\overline{u}_z) = 0. \quad \text{(A4)}$$

In the quasigeostrophic approximation, for which $\zeta/f \equiv R_o \ll 1$ and the characteristic "x" and "y" length scales of the geostrophic flow field are nearly equal, $(\overline{w}_x, \overline{w}_y, \overline{w}_z)/f \sim O[R_o^2(H/L, H/L, 1)]$. At lowest order, (A4) reduces to

$$\alpha = \pm(S_n^2 + S_s^2 - \zeta^2)^{1/2}/2, \quad \text{(A5)}$$

in which

$$\zeta \equiv \overline{v}_x - \overline{u}_y,$$
$$S_n \equiv \overline{u}_x - \overline{v}_y,$$
$$S_s \equiv \overline{v}_x + \overline{u}_y,$$
$$\Delta \equiv \overline{v}_x + \overline{u}_y, \quad \text{(A6)}$$

the variables S_n and S_s represent normal and shear components of the rate of strain tensor, ζ is relative vorticity, and Δ is the horizontal divergence.

The phenomenology of (A5) is simple. Solutions to (A5) represent exponential growth and decay if $S_n^2+S_s^2>\zeta^2$ and have an oscillatory component otherwise.

WAVE CAPTURE

Jones (1969) and Bühler and McIntyre (2005) further argue for a shrinking catastrophe or wave capture scenario. Because

$$\frac{dm}{dt} = -k\overline{u}_z - l\overline{v}_z,$$

an exponential increase of k_h corresponds to an exponential increase/decrease of m, depending on the sign of $(\overline{u}_z, \overline{v}_z)$ relative to the horizontal wavevector (k, l). Those waves with a growing vertical wavenumber will tend to be captured within the extensive regions of the eddy strain field and will eventually dissipate, leading Bühler and McIntyre (2005) to characterize the interaction as a nontrivial variant of critical layer behavior. A captured wave with exponentially growing horizontal and vertical wavenumbers will asymptotically tend to a superinertial intrinsic frequency that depends on the aspect ratio of the background flow (3).

b. Symmetric (2D) backgrounds

Internal wave–mean flow interactions are qualitatively different for symmetric flows such as a zonal jet with $(\overline{u}, \overline{v})=[\overline{u}(y, z), 0]$ or an axisymmetric vortex. While one can derive wave equations for such flows without going into the low R_o, F_r parameter regime and without the requirement of a scale separation, the impact of symmetry on behavior is best appreciated in those limits. Componentwise for the wavevector (k, l, m) in a zonal $[\overline{u}(y, z)]$ flow,

$$\frac{dk}{dt} = 0,$$
$$\frac{dl}{dt} = -k\overline{u}_y,$$
$$\frac{dm}{dt} = -k\overline{u}_z. \quad \text{(A7)}$$

The zonal wavenumber is constant. Differentiating with respect to time returns the result that the meridional and vertical wavenumbers grow linearly in time.

CRITICAL LAYERS

Critical layer behavior is exhibited as a wave packet, having constant zonal wavenumber (k) and Eulerian frequency σ, and evolves through vertical propagation in a sheared flow $\overline{u}(z)$, such that the intrinsic frequency

$$\omega = \sigma - k\overline{u} \to f$$

tends to f.

c. Near-inertial internal wave trapping

The interaction between internal waves and geostrophically balanced background flows discussed so far has only been through the Doppler shift. An added layer of complexity happens when one relaxes the scale separation requirement and introduces mean flow gradients directly into the dispersion relation. Kunze (1985) produces a dispersion relation by taking the determinant of the linearized equations of motion. This procedure systematically neglects gradients of Doppler shifting that are the same order of magnitude as the background gradients that Kunze (1985) is attempting to introduce into the dispersion relation (Polzin et al. 1996). Kunze's (1985) dispersion relation,

$$\omega \cong f + \zeta/2 + \frac{N^2k_h^2}{2fm^2} + \frac{1}{m}(l\overline{u}_z - k\overline{v}_z), \quad \text{(A8)}$$

is not correct at $O(F_r)$. The expression (A8) was used in conjunction with ray-tracing arguments to explain an observed correlation between energy and relative vorticity in an upper ocean frontal regime (Kunze and Sanford 1984). Kunze et al. (1995) and Kunze and Toole (1997) have used this approach to explain observations

of nominally subinertial ($f + \zeta/2 < \omega < f$) internal waves having a negligible Doppler shift in symmetric background flows (a warm core ring and the vortex cap atop Fieberling Guyot). These examples can be seen as special cases of wave–mean interactions for which the proposed dispersion relation (A8) reduces to that consistent with solutions to a wave equation (Kunze and Boss 1998). The critical layer in this problem is provided by the variation of the relative vorticity ζ.

d. Spontaneous imbalance

Ray tracing is based on the continuity of a real-valued phase function Ω. As one reaches the $(R_o, F_r) \sim O(1)$ region of parameter space, a geostrophically balanced flow field can either spontaneously degenerate into internal waves through ageostrophic instabilities (Molemaker et al. 2005), implying a complex frequency, or otherwise be considered to force the internal wave field (Ford et al. 2000). In either case, the transfer of energy and momentum from balanced to unbalanced motions is believed to be weak in the small Rossby number, Froude number limit.

Those analyses, however, do not consider the effects of Doppler shifting, and it is worth considering what happens to (A4) as the $[R_o, F_r \sim O(1)]$ parameter space is approached. In this instance, the factors in (A3) involving the vertical velocity gradients are not small. The prefactor multiplying α becomes

$$S_n^2 + S_s^2 - \zeta^2 \to \sum_{i=1}^{3} S_{ni}^2 + S_{si}^2 - \zeta_i^2 - \Delta_i^2, \quad \text{(A9)}$$

in which the subscript $i = 1 \to 3$ denotes the $x - z$, $y - z$ and $x - y$ planes. Beyond noting that $\overline{w}_z(\overline{u}_x\overline{v}_y - \overline{v}_x\overline{u}_y) = \Delta(S_n^2 + S_s^2 - \zeta^2 - \Delta^2)$, (A3) appears not to admit to a simple characterization: strain, vorticity, and divergence in all three planes can be significant.

REFERENCES

Bendat, J. S., and A. G. Piersol, 1986: Random data. *Analysis and Measurement Procedures,* 2nd ed. John Wiley & Sons.

Bretherton, F. P., 1966: The propagation of groups of internal gravity waves in a shear flow. *Quart. J. Roy. Meteor. Soc.,* **92,** 466–480.

——, 1969: On the mean motion induced by internal gravity waves. *J. Fluid Mech.,* **36,** 785–803.

Brown, E. D., and W. B. Owens, 1981: Observations of the horizontal interactions between the internal wave field and the mesoscale flow. *J. Phys. Oceanogr.,* **11,** 1474–1480.

Bryden, H. L., 1982: Sources of eddy energy in the Gulf Stream Recirculation Region. *J. Mar. Res.,* **40,** 1047–1068.

Bühler, O., and M. E. McIntyre, 2005: Wave capture and wave-vortex duality. *J. Fluid Mech.,* **534,** 67–95.

Cairns, J. L., and G. O. Williams, 1976: Internal wave observations from a midwater float, 2. *J. Geophys. Res.,* **81,** 1943–1950.

D'Asaro, E. A., 1995: Upper-ocean inertial currents forced by a strong storm. Part III: Interaction of inertial currents and mesoscale eddies. *J. Phys. Oceanogr.,* **25,** 2953–2958.

Ford, R., M. E. McIntyre, and W. A. Norton, 2000: Balance and the slow quasimanifold: Some explicit results. *J. Atmos. Sci.,* **57,** 1236–1254.

Freeland, H. J., and W. J. Gould, 1976: Objective analysis of mesoscale ocean circulation features. *Deep-Sea Res.,* **23,** 915–923.

Garrett, C., and W. Munk, 1975: Space-time scales of internal waves: A progress report. *J. Geophys. Res.,* **80,** 291–297.

Jones, W. L., 1967: Propagation of internal gravity waves in fluids with shear flow and rotation. *J. Fluid Mech.,* **30,** 439–448.

——, 1969: Ray tracing for internal gravity waves. *J. Geophys. Res.,* **74,** 2028–2033.

Joyce, T. M., and M. C. Stalcup, 1984: An upper ocean current jet and internal waves in a Gulf Stream Warm Core Ring. *J. Geophys. Res.,* **89,** 1997–2003.

Kunze, E., 1985: Near-inertial wave propagation in geostrophic shear. *J. Phys. Oceanogr.,* **15,** 544–565.

——, and T. B. Sanford, 1984: Observations of near-inertial waves in a front. *J. Phys. Oceanogr.,* **14,** 566–581.

——, and J. M. Toole, 1997: Tidally driven vorticity, diurnal shear, and turbulence atop Fieberling Seamount. *J. Phys. Oceanogr.,* **27,** 2663–2693.

——, and E. Boss, 1998: A model for vortex-trapped internal waves. *J. Phys. Oceanogr.,* **28,** 2104–2115.

——, R. W. Schmitt, and J. M. Toole, 1995: The energy balance in a warm-core ring's near-inertial critical layer. *J. Phys. Oceanogr.,* **25,** 942–957.

Leaman, K. D., 1976: Observations on the vertical polarization and energy flux of near-inertial waves. *J. Phys. Oceanogr.,* **6,** 894–908.

——, and T. B. Sanford, 1975: Vertical energy propagation of inertial waves: A vector spectral analysis of velocity profiles. *J. Geophys. Res.,* **80,** 1975–1978.

Lee, V., and C. Wunsch, Eds., 1977: *Atlas of the Mid-Ocean Dynamics Experiment (MODE-I).* MIT, 274 pp.

McWilliams, J. C., 1976: Maps from the Mid-Ocean Dynamics Experiment. Part I: Geostrophic streamfunction. *J. Phys. Oceanogr.,* **6,** 810–827.

Mied, R. P., G. J. Lindemann, and C. L. Trump, 1987: Inertial wave dynamics in the North Atlantic Subtropical Zone. *J. Geophys. Res.,* **92,** 13 063–13 074.

——, C. Y. Shen, and M. J. Kidd, 1990: Current shear-inertial wave interaction in the Sargasso Sea. *J. Phys. Oceanogr.,* **20,** 81–96.

Molemaker, M. J., J. C. McWilliams, and I. Yavneh, 2005: Baroclinic instability and loss of balance. *J. Phys. Oceanogr.,* **35,** 1505–1517.

Müller, P., 1976: On the diffusion of momentum and mass by internal gravity waves. *J. Fluid Mech.,* **77,** 789–823.

Ooyama, K., 1966: On the stability of the baroclinic circular vortex: A sufficient criterion for instability. *J. Atmos. Sci.,* **23,** 43–53.

Polzin, K. L., 2004: A heuristic description of internal wave dynamics. *J. Phys. Oceanogr.,* **34,** 214–230.

——, J. M. Toole, and R. W. Schmitt, 1995: Finescale parameterizations of turbulent dissipation. *J. Phys. Oceanogr.,* **25,** 306–328.

——, N. S. Oakey, J. M. Toole, and R. W. Schmitt, 1996: Fine-structure and microstructure characteristics across the northwest Atlantic Subtropical Front. *J. Geophys. Res.,* **101,** 14 111–14 121.

——, E. Kunze, J. M. Toole, and R. W. Schmitt, 2003: The partition of fine-scale energy into internal waves and subinertial motions. *J. Phys. Oceanogr.,* **33,** 234–248.

Provenzale, A., 1999: Transport by coherent barotropic vortices. *Ann. Rev. Fluid Mech.,* **31,** 55–93.

Sanford, T. B., 1975: Observations of the vertical structure of internal waves. *J. Geophys. Res.,* **80,** 3861–3871.

Shephard, T. G., 1990: Symmetries, conservation laws, and Hamiltonian structure in geophysical fluid dynamics. *Advances in Geophysics,* Vol. 32, Academic Press, 287–338.

Weller, R. A., 1982: The relation of near-inertial motions observed in the mixed layer during the JASIN (1978) experiment to the local wind stress and to the quasi-geostrophic flow field. *J. Phys. Oceanogr.,* **12,** 1122–1136.